
GRADIENT-FREE AEROACOUSTIC SHAPE OPTIMIZATION USING LARGE EDDY SIMULATION

A PREPRINT

Mohsen Hamedi and Brian C. Vermeire

*Department of Mechanical, Industrial, and Aerospace Engineering
Concordia University
Montréal, QC, Canada*

December 25, 2023

ABSTRACT

We present an aeroacoustic shape optimization framework that relies on high-order Flux Reconstruction (FR) spatial discretization, the gradient-free Mesh Adaptive Direct Search (MADS) optimization algorithm, and Large Eddy Simulation (LES). Our parallel implementation ensures that the runtime of each optimization iteration remains consistent, irrespective of the number of design parameters involved in the optimization problem, provided sufficient resources are available. This eliminates the dependence of the runtime of gradient-free algorithms on the number of design variables. The objective is to minimize Sound Pressure Level (SPL) at a near-field observer by computing it directly from the flow field. We evaluate this framework across three different problems. First, an open deep cavity is considered at a free-stream Mach number of $M_\infty = 0.15$ and Reynolds number of $Re = 1500$ based on the cavity's depth, reducing the SPL by 12.86 dB. Next, we optimized tandem cylinders at $Re = 1000$ and $M_\infty = 0.2$, achieving over 11 dB noise reduction by optimizing cylinder spacing and diameter ratio. Lastly, a baseline NACA0012 airfoil is optimized at $Re = 23000$ and $M_\infty = 0.2$. The airfoil's shape is optimized to generate a new 4-digit NACA airfoil at an appropriate angle of attack to minimize the SPL while ensuring the baseline time-averaged lift coefficient is maintained and prevent any increase in the baseline time-averaged drag coefficient. The SPL is reduced by 5.66 dB while the mean drag coefficient is reduced by more than 7%. These results highlight the feasibility and effectiveness of our aeroacoustic shape optimization framework.

Keywords: *Aeroacoustics; Gradient-Free; Optimization; High-Order; Large Eddy Simulation.*

1 INTRODUCTION

The World Health Organization (WHO) estimates an annual loss of over a million healthy life years in Western Europe due to noise-induced diseases [1]. The adverse impacts of noise on the environment and human health have been well established [2, 3]. Environmental impacts include disruptions to wildlife behaviour and habitat [4], while human health impacts can range from hearing loss and sleep disturbance to increased stress levels and cardiovascular diseases [3]. To address these critical issues, it is imperative to reduce noise pollution, highlighting the need to develop aeroacoustic optimization frameworks.

Aeroacoustic optimization has received significant attention in recent years due to its various applications, such as reducing wind turbine noise for widespread deployment, minimizing aviation noise to enhance the comfort of communities near airports, and designing quiet air taxis for urban air mobility, among others. An aeroacoustic shape optimization framework comprises three distinct components. Initially, a flow solver is utilized to capture aerodynamic flow characteristics. Subsequently, an acoustic solver computes noise at the observer(s) based on the acquired aerodynamic flow data, which is omitted in the direct acoustic approach, wherein noise is directly computed within the flow solver. The final component is the optimization algorithm, responsible for identifying candidate designs for each optimization iteration. Various aeroacoustic optimization frameworks are constructed by employing different methods for each of these components.

XFOIL simulations have found extensive application in aeroacoustic shape optimization for aerodynamic analysis [5, 6, 7]. While optimization frameworks employing panel methods offer cost-effective exploration of design spaces, panel methods may lack the precision needed for reliably obtaining optimal designs [6]. Thus, more reliable methods should be considered to find optimal designs. An alternative to panel methods is Reynolds-Averaged Navier-Stokes (RANS) simulations, which have previously been used for aeroacoustic shape optimization [8, 9, 10, 11, 12]. However, due to the inherent unsteady nature of noise phenomena, the RANS approach can add unwanted dissipation of broadband noise [13]. Consequently, scale-resolving techniques, i.e., Large Eddy Simulation (LES), Implicit LES (ILES), and Direct Numerical Simulation (DNS) are of interest. They offer an unsteady and detailed representation of the flow physics and resulting acoustic waves, and are appealing alternatives, albeit with added computational cost [14, 15, 16].

The majority of Computational Fluid Dynamics (CFD) codes for simulating unsteady compressible flow, such as OpenFOAM [17], SU2 [18, 19], and CHARLES [20], rely on Finite Volume (FV) methods with second-order spatial accuracy. While these methods can handle complex geometries on unstructured meshes and scale to approximately one million cores [21], they are constrained by a low FLOPS-to-bytes ratio and high indirect memory access, preventing them from fully harnessing the computational power of modern hardware platforms [22]. As specified by CFD 2030 Vision study by the National Aeronautics and Space Administration (NASA) [13], CFD techniques for LES/DNS must adapt to a paradigm shift in High-Performance Computing (HPC) hardware. The industry-standard FV methods only achieve 3% of the theoretical peak performance on modern hardware architectures [23]; however, the FR approach [24] is capable of achieving over 55% [22]. In addition, the FR approach has been shown to be suitable for scale-resolving

simulations, leveraging the behaviour of its numerical error for ILES [25], and via filtering approaches for highly under-resolved problems [26]. Thus, FR proves computationally superior to lower-order FV techniques, with reduced numerical dispersion and dissipation errors on a per degree of freedom basis [27, 28, 29]. In this study, our High-ORder Unstructured Solver (HORUS) is used, which employs the FR approach for spatial discretization of the governing equations with ILES for sub-grid scale modelling.

The emergence of adjoint-based optimization methods [30, 31], characterized by computational cost independence from the number of design variables, has enabled the exploration of large-scale practical problems in aerodynamic optimization [32]. While a substantial body of literature focuses on steady-state problems, the unsteady nature of numerous aerospace problems, such as aeroacoustics, has received less attention in adjoint-based optimization due to the considerable storage requirements for solving unsteady adjoint equations [33] and their unconditional instability for chaotic systems [34]. A more robust alternative for aeroacoustic shape optimization using LES is the gradient-free Mesh Adaptive Direct Search (MADS) algorithm [35, 36]. The suitability of MADS, coupled with HORUS, has been demonstrated in the works of Karbasian and Vermeire [37] and Aubry et al. [38] for aerodynamic shape optimization, and by Hamed and Vermeire [39] for laminar aeroacoustic shape optimization.

In this study, we introduce an aeroacoustic shape optimization framework based on the FR approach and the gradient-free MADS optimization algorithm for LES. Building upon our prior work [39], which assessed this framework for two-dimensional problems at low Reynolds numbers, we extend its application to three-dimensions. To the best of our knowledge, no other studies have integrated the gradient-free MADS optimization with a high-order LES solver. One significant limitation of the MADS algorithm is its computational cost, which scales with the number of design parameters, necessitating a corresponding number of CFD simulations in each optimization iteration. However, our proposed optimization framework is implemented in parallel, enabling all CFD simulations to run concurrently during each iteration, rendering the computational cost of this framework independent of the number of design parameters, provided sufficient computing resources are available.

This paper is outlined as follows. The methodology is given in Section 2. Then, shape of a three-dimensional open cavity is optimized to reduce noise in Section 3, followed by three-dimensional tandem cylinders in Section 4, and, airfoil shape optimization for noise reduction is performed in Section 5. Finally, the conclusions and recommendations for future work are given in Section 6.

2 METHODOLOGY

This section presents an overview of the methodology employed to solve the unsteady Navier-Stokes equations along with the aeroacoustic shape optimization framework.

2.1 GOVERNING EQUATIONS

The compressible unsteady Navier-Stokes equations can be cast in the following general form

$$\frac{\partial \mathbf{u}}{\partial t} + \nabla \cdot \mathbf{F} = 0, \quad (1)$$

where t is time and \mathbf{u} is a vector of conserved variables

$$\mathbf{u} = \begin{bmatrix} \rho \\ \rho u_i \\ \rho E \end{bmatrix}, \quad (2)$$

where ρ is density, ρu_i is a component of the momentum, u_i are velocity components, and ρE is the total energy. The inviscid and viscous Navier-Stokes fluxes are

$$\mathbf{F}_{inv,j}(\mathbf{u}) = \begin{bmatrix} \rho u_j \\ \rho u_i u_j + \delta_{ij} p \\ u_j (\rho E + p) \end{bmatrix}, \quad (3)$$

and

$$\mathbf{F}_{vis,j}(\mathbf{u}, \nabla \mathbf{u}) = \begin{bmatrix} 0 \\ \tau_{ij} \\ -q_j - u_i \tau_{ij} \end{bmatrix}, \quad (4)$$

respectively, where δ_{ij} is the Kronecker delta. The pressure is determined via the ideal gas law as

$$p = (\gamma - 1) \rho \left(E - \frac{1}{2} u_k u_k \right), \quad (5)$$

where $\gamma = 1.4$ is the ratio of the specific heat at constant pressure, c_p , to the specific heat at constant volume, c_v . The viscous stress tensor is

$$\tau_{ij} = \mu \left(\frac{\partial u_i}{\partial x_j} + \frac{\partial u_j}{\partial x_i} - \frac{2}{3} \frac{\partial u_k}{\partial x_k} \delta_{ij} \right), \quad (6)$$

and, the heat flux is

$$q_j = -\frac{\mu}{Pr} \frac{\partial}{\partial x_j} \left(E + \frac{p}{\rho} - \frac{1}{2} u_k u_k \right), \quad (7)$$

where μ is the dynamic viscosity and $Pr = 0.71$ is the Prandtl number.

2.2 FLOW SOLVER

The in-house solver, HORUS, is utilized for solving the Navier-Stokes equations, employing the FR approach for spatial discretization. More comprehensive details about the FR approach for multiple dimensions are provided in the following section. The second-order accurate Nasab-Pereira-Vermeire scheme [40], which incorporates an adaptive time-stepping method [41], is used to advance the solution in time throughout this study.

2.2.1 FLUX RECONSTRUCTION

The FR approach is used to discretize the divergence operator for general advection-diffusion equations of the form shown in Equation 1. It is a high-order accurate numerical method first introduced by Huynh [24] in 2007, and extended to multi-dimensions for mixed element types by Wang and Gao [42]. FR is appealing due to its accuracy, generality, robustness, and suitability for modern hardware architectures [22]. Compared to commonly-used low-order numerical methods, FR provides more accurate solutions using fewer degrees of freedom and at reduced computational cost [43]. The FR framework is outlined here in multiple dimensions, following Wang’s formulation [42].

In the FR approach, the computational domain, Ω , is discretized into a mesh of N_e non-overlapping elements such that

$$\Omega = \bigcup_{k=1}^{N_e} \Omega_k, \quad \bigcap_{k=1}^{N_e} \Omega_k = \emptyset. \quad (8)$$

Each element, Ω_k , contains a number of solution points based on the desired solution polynomial degree. For the sake of simplicity, these elements are transformed from the physical space \mathbf{x} to a standard reference space $\boldsymbol{\xi}$, where \mathbf{x} and $\boldsymbol{\xi}$ are the spatial coordinates in the physical and reference spaces, respectively. The transformation of these elements is performed via an invertible mapping function, M , such that

$$\mathbf{x} = M(\boldsymbol{\xi}) \iff \boldsymbol{\xi} = M^{-1}(\mathbf{x}). \quad (9)$$

The Jacobian of this mapping can be found at any point from

$$J = \frac{\partial \mathbf{x}}{\partial \boldsymbol{\xi}}, \quad (10)$$

which enables all element operations to be performed on the same reference element and, upon completion, mapped back to physical space.

In this study, the solution and flux points are located at tensor products of Gauss points for hexagonal elements. The solution is approximated at each solution point, and then, the solution polynomial within each element is interpolated using nodal basis functions, ensuring element-wise continuity of the solution,

$$\mathbf{u}_k^\delta(\boldsymbol{\xi}, t) = \sum_{i=1}^{N_p} \mathbf{u}_{k,i}^\delta \phi_i(\boldsymbol{\xi}), \quad (11)$$

where $\mathbf{u}_{k,i}^\delta$ is the numerical solution at point i within element Ω_k , N_p is the total number of solution points within the element Ω_k , and $\phi_i(\boldsymbol{\xi})$ is the nodal basis function at point i . Furthermore, the flux polynomial is interpolated using nodal basis functions

$$\mathbf{F}_k^{\delta D}(\boldsymbol{\xi}, t) = \sum_{i=1}^{N_p} F_{k,i}^\delta \phi_i(\boldsymbol{\xi}), \quad (12)$$

where $F_{k,i}^\delta = f(U_{k,i}^\delta, \nabla U_{k,i}^\delta)$ is the numerical flux value at point i within element Ω_k . The constructed numerical flux function, $\mathbf{F}_k^{\delta D}(\boldsymbol{\xi}, t)$, is allowed to be discontinuous across cell interfaces, and the superscript D denotes this discontinuity.

Thus, a common Riemann flux must be defined to replace the normal flux. In this study, a Rusanov/Lax-Friedrichs flux is used at the interface between elements. To account for the jumps across cells, we follow Wang's formulation [42] for simplex elements. By defining a correction field, $\vartheta_k \in \mathbb{P}^p$, Equation 1 is re-written within each element and must be satisfied at each solution point, i.e.,

$$\frac{d\mathbf{u}_{k,i}^\delta}{dt} + (\nabla \cdot \mathbf{F}_k^\delta)_{\xi_{k,i}} + \vartheta_{k,i} = 0. \quad (13)$$

The correction field ensures a globally continuous flux polynomial and can be determined for each solution point, i , within element k , by

$$\vartheta_{k,i} = \frac{1}{|\Omega_k|} \sum_{f \in \partial\Omega_k} \sum_j \alpha_{i,f,j} [\tilde{\mathbf{F}}]_{f,j} S_f, \quad (14)$$

where f denotes the faces of the element Ω_k , j is the index for flux points, $\alpha_{i,f,j}$ are constant lifting coefficients, $[\tilde{\mathbf{F}}]_{f,j}$ is the difference between a common Riemann flux at point j and the value of the internal flux, and S_f is the area of the face f . The lifting coefficients are computed using a weighting function, W , and are independent of both geometry and the solution [42]. In this study, the DG method is recovered via the FR formulation by choosing nodal basis functions as the weighting function [42], and the Rusanov and second method of Bassi and Rebay (BR2) are used for the common inviscid and viscous flux.

2.3 OPTIMIZATION FRAMEWORK

In this study, we employ the minimal bases construction of the MADS optimization technique, similar to our previous work [39], for aeroacoustic shape optimization of the open deep cavity and tandem cylinders. However, when optimizing NACA 4-digit airfoils, we have devised a parallel optimization framework, utilizing the maximal bases construction of the OrthoMADS algorithm [36], to mitigate the computational cost associated with serial MADS optimization.

The optimization framework starts with a baseline design. Initially, HORUS is used to simulate the baseline design, and the objective function is evaluated. Subsequently, the MADS algorithm identifies candidate designs for optimization iterations, and these designs are simulated using HORUS, followed by objective function evaluation. This process continues until convergence criteria are satisfied. The MADS algorithm used in this study is explained in details in the following section and Algorithm 1.

2.3.1 MESH ADAPTIVE DIRECT SEARCH

The MADS algorithm falls between the Generalized Pattern Search (GPS) [44] and the Coope and Price frame-based methods [45]. Unlike GPS, MADS allows for more flexible exploration of the design space during the optimization process, which makes it a more effective solution for both unconstrained and linearly constrained optimization [35]. A major advantage of MADS over GPS is the flexible local exploration, known as poll directions, rather than a fixed set of directions. Two parameters are defined in the context of the MADS optimization: the mesh size parameter, Δ^m , and the poll size parameter, Δ^p . The mesh size parameter determines the granularity and resolution of the mesh of the design

space on which the optimization algorithm operates. A higher resolution leads to a more precise search while a lower resolution allows for a wider search and a higher chance of finding the global optimal solution. The poll size determines the size of the neighbourhood around the incumbent point where new trial points are chosen. The number of trial points in each optimization iteration can be either $n + 1$, known as minimal positive basis, or $2n$, known as maximal positive basis [35], where n is the number of design variables.

In the gradient-free MADS optimization procedure, there are two sequential steps in each design iteration, the search step, and the poll step. The optimization procedure begins with the search step and the initial design point, $\mathbf{X}_0 = [\mathcal{X}_0^1, \mathcal{X}_0^2, \dots, \mathcal{X}_0^n]$, where the subscript is the optimization iteration and the superscript denotes each design parameter. A finite number of trial points are defined, and infeasible ones are discarded. Infeasible trial points are points within the design space that do not satisfy the constraints of the optimization problem. The trial points are generated based on the current mesh and the direction vectors, $\mathbf{d}_j \in \mathcal{D}$ (for $j = 1, 2, \dots, n$), where \mathcal{D} is the design space. \mathcal{D} must be a positive spanning set [46], and each direction, \mathbf{d}_j , must be the product of some fixed non-singular generating matrix by an integer vector [35]. In the OrthoMADS algorithm, the polling directions are orthogonal to each other and the mesh at iteration k is defined as [35]

$$\mathcal{M}_k = \bigcup_{\mathcal{X} \in \mathcal{S}_k} \{\mathcal{X} + \Delta_k^m \mathcal{D}z : z \in \mathbb{N}^{n_{\mathcal{D}}}\}, \quad (15)$$

where \mathcal{S}_k is the set of trial points that the objective function is evaluated at, in iteration k . The mesh \mathcal{M}_k is constructed from a finite set of $n_{\mathcal{D}}$ directions, $\mathcal{D} \subset \mathbb{R}^n$, scaled by a mesh size parameter $\Delta_k^m \in \mathbb{R}_+$. The objective function is evaluated at these trial points. The current iteration stops after the objective function at all trial points is computed. Then, the next iteration starts with a new incumbent solution $\mathbf{X}_{k+1} \in \Omega$ with objective function of $\mathcal{F}(\mathbf{X}_{k+1}) < \mathcal{F}(\mathbf{X}_k)$, and a mesh size parameter $\Delta_{k+1}^m \geq \Delta_k^m$. The maximum value of the mesh size parameter, at any iteration, is set to one, $\Delta_{max}^m = 1$. Note that the design space of each design variable is scaled to one, and a mesh size parameter of one can cover the entire design space.

On the other hand, if the search step fails in finding a new optimum, the poll step is invoked before terminating the current optimization iteration. In the poll step, the mesh size parameter is reduced to define a new set of trial points closer to the incumbent design variables. The key difference between GPS and MADS is the new poll size parameter, $\Delta_k^p \in \mathbb{R}_+$, that controls the magnitude of the distance between trial points generated by the poll step to the incumbent point. This new set of trial points defined in the poll step is called a frame. The MADS frame at iteration k is defined to be [35]

$$P_k = \{\mathcal{X}_k + \Delta_k^m d : d \in \mathcal{D}_k\} \subset \mathcal{M}_k, \quad (16)$$

where \mathcal{D}_k is a positive spanning set. In each iteration, the mesh and poll size parameters are defined. The mesh size parameter of the new iteration is defined as [35]

$$\Delta_{k+1}^m = \begin{cases} \frac{1}{4}\Delta_k^m & \text{if the poll step fails to find an improved design point,} \\ 4\Delta_k^m & \text{if an improved design point is found, and if } \Delta_k^m \leq \frac{1}{4}, \\ \Delta_k^m & \text{otherwise.} \end{cases} \quad (17)$$

These rules ensure Δ_k^m is always a power of 4 and never exceeds 1. The poll size parameter is also defined as [35]

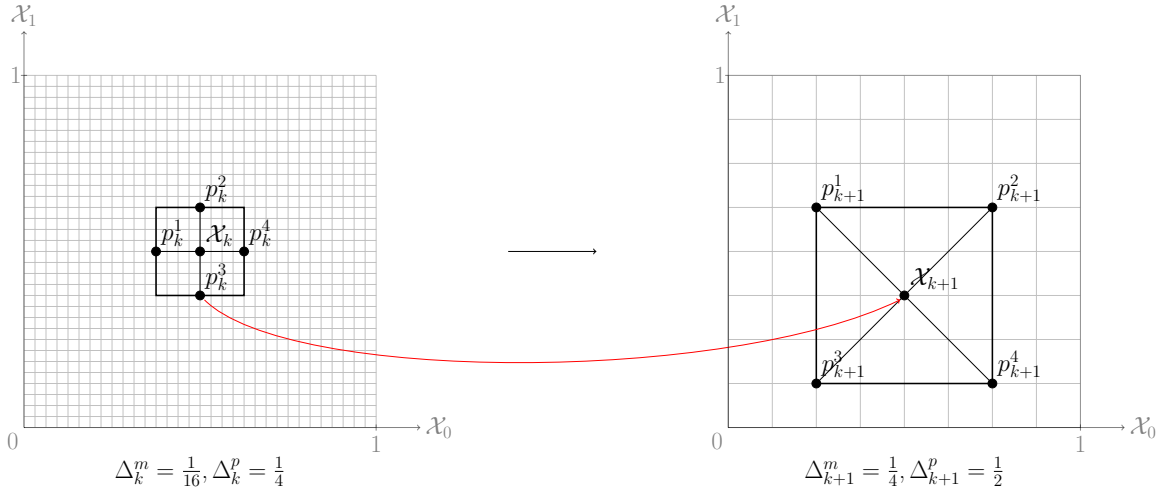
$$\Delta_{k+1}^p = \begin{cases} n\sqrt{\Delta_k^m} & \text{if the minimal positive basis construction is used,} \\ \sqrt{\Delta_k^m} & \text{if the maximal positive basis construction is used.} \end{cases} \quad (18)$$

The search and poll steps are depicted in Figure 1 for a scaled design space with two design variables. In this example, the maximal positive basis construction results in four trial points per iteration. The current incumbent design point is \mathbf{X}_k and the trial points, p_k^1, p_k^2, p_k^3 , and p_k^4 are chosen in the specified frame defined via the poll size parameter. The objective function is computed at these trial points, and we assume the p_k^3 trial point is the new incumbent design point. Then, the search is successful and the mesh size parameter is quadrupled. However, on the other hand, if a new incumbent design point is not found, the search step is unsuccessful, and the poll step is invoked, as depicted in Figure 1b. In the poll step, the mesh size parameter is reduced by a factor of four to define a new set of trial points closer to the incumbent design. Then, the objective function is evaluated at these trial points. Finally, the optimization problem is terminated when the stopping criteria are met.

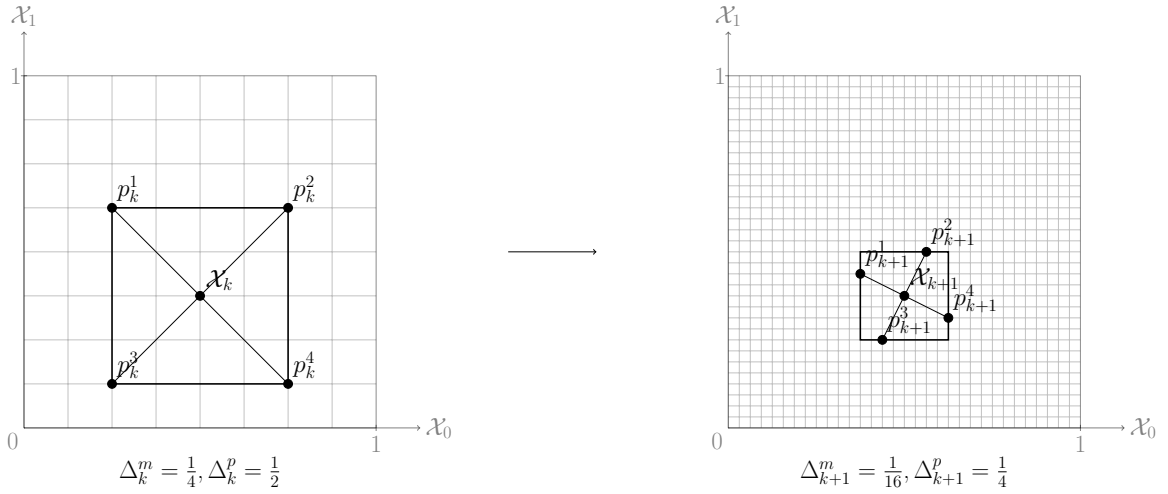
In this study, the optimization process stops when the mesh size parameter falls below 10^{-6} , and the changes in design parameter values between two consecutive iterations are less than one percent. These criteria indicate the algorithm has successfully converged to an optimal design. The algorithm for the proposed aeroacoustic shape optimization framework is presented in Algorithm 1. Notably, the for loop in line 18 is the most computationally intensive part of the algorithm where a total of n CFD simulations are conducted. Typically, each CFD simulation runs in parallel, and trial designs are executed sequentially. However, in the proposed parallel implementation of the algorithm, all trial designs run concurrently, reducing the runtime of n CFD simulations to that of a single CFD simulation, provided ample computer resources are available.

3 DEEP CAVITY

Flow over an open deep cavity is a classical problem in fluid mechanics and aeroacoustics, and has been the subject of extensive research due to its relevance for a range of engineering applications. The flow over a cavity is characterized by a complex interplay between the boundary layer, the recirculation zone inside the cavity, and the external flow. The occurrence of self-sustained oscillations of velocity and pressure can induce acoustic noise or strong vibrations. The presence of the cavity can lead to a variety of aerodynamic and aeroacoustic phenomena, such as flow separation,



(a) Successful search step.



(b) Poll step as a result of unsuccessful search step.

 Figure 1. Search and poll steps of the OrthoMADS optimization techniques for iteration k .

Algorithm 1: The aeroacoustic shape optimization framework.

```

1  $k = 0$ ;
2 MADS Iteration,  $iter = 0$ ;
3 Run Baseline Design;
4 Evaluate  $\mathcal{F}_0$ ;
5 Define Incumbent  $\mathcal{I}_0 = \mathcal{F}_0$ ;
6 Define  $\Delta_0^m$ ;
7 while True do
8   if  $\Delta_k^m > \Delta_0^m$  then
9      $\Delta_k^m = \Delta_0^m$ ;
10  end
11  if minimal positive basis construction then
12     $\Delta_k^p = n \sqrt{\Delta_k^m}$ ;
13  end
14  if maximal positive basis construction then
15     $\Delta_k^p = \sqrt{\Delta_k^m}$ ;
16  end
17  Identify Trial Designs,  $\mathbf{p}_k^1, \dots, \mathbf{p}_k^n$ ;
18  for  $i = 1, \dots, n$  do
19    Run HORUS for  $\mathbf{p}_k^i$ ;
20    Evaluate  $\mathcal{F}_k^i$ ;
21  end
22  if  $\min\{\mathcal{F}_k^1, \dots, \mathcal{F}_k^n\} < \mathcal{I}_{iter}$  then
23     $\Delta_{k+1}^m = 4\Delta_k^m$ ;
24     $iter += 1$ ;
25     $\mathcal{I}_{iter} = \min\{\mathcal{F}_k^1, \dots, \mathcal{F}_k^n\}$ ;
26  else
27     $\Delta_{k+1}^m = \frac{1}{4}\Delta_k^m$ ;
28  end
29   $k += 1$ ;
30  if  $\Delta_k^m < 10^{-6}$  and  $\left| \frac{\mathbf{X}_k - \mathbf{X}_{k-1}}{\mathbf{X}_{k-1}} \right| < 0.01$  then
31    break;
32  end
33 end

```

unsteady vortex shedding, and acoustic resonance. Understanding the aerodynamic and aeroacoustic characteristics of flow over a cavity is crucial for optimizing the design and performance of many engineering systems.

Extensive research has been conducted on two-dimensional cavity flows, leading to favorable agreement between experimental data and numerical two-dimensional simulations. While three-dimensionality is observed in cavity flow experiments, it underscores the significance of conducting three-dimensional cavity flow simulations [47, 48]. Lawson [49] reviewed the experimental and numerical studies of open cavities. Furthermore, the radiated noise from cavity is studied via LES by several researchers [50, 51, 52, 53]. The geometry of a three-dimensional cavity is usually given in terms of length-to-depth, L/D , and width-to-depth, W/D , ratios, as depicted in Figure 2. In this section, flow over an open cavity is validated and then the noise at a near-field observer is minimized via the proposed gradient-free shape optimization framework.

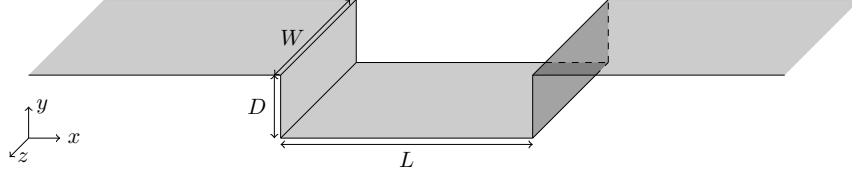


Figure 2. The geometry of the three-dimensional open deep cavity.

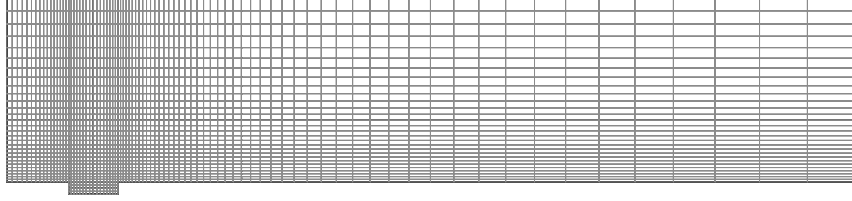


Figure 3. The mesh of the three-dimensional open deep cavity.

3.1 VALIDATION

In this section, we extend our previous work [39] by extruding it in the z -direction. The grid convergence study is performed using the time-averaged drag coefficient, and sound pressure level measured at an observer located $7.16D$ above the cavity's center.

3.1.1 COMPUTATIONAL DETAILS

To be consistent with [39], the open cavity with a length-to-depth ratio of $L/D = 4$ is extruded in the z -direction with a width-to-depth ratio of $W/D = 3$. The Reynolds number, based on the depth of the cavity, is $Re_D = 1500$, and the Mach number is 0.15. To ensure wake mode oscillations, the inlet boundary is placed $5D$ upstream of the cavity inlet, resulting in a boundary layer thickness of $\delta/D \approx 0.2$ at the entrance of the cavity. The outflow boundary is placed $60D$ downstream of the cavity's trailing edge wall, with the last $50D$ acting as a buffer region to eliminate acoustic wave reflections. The computational domain extends to $15D$ in the y -direction with the last $5D$ as a buffer region. The grid stretching ratio is 1.05 and 1.075 for the resolved and buffer regions, respectively, with a minimum element size of $0.2D$ inside the cavity. A total of 14,652 hexagonal elements are used. The geometry and mesh of the three-dimensional cavity are shown in Figures 2 and 3, respectively. The periodic boundary condition is used in the spanwise direction, no-slip boundary conditions are applied at the walls, and Riemann invariant boundary conditions are applied at the inlet and outlet of the computational domain. The simulation is run for $100t_c$, where $t_c = D/U_\infty$, to allow initial transients to disappear and then run for another $400t_c$ to average the statistical quantities. To ensure uncorrelated turbulent fluctuations at a separation of half the domain size, the correlation coefficient of the x -component of the velocity perturbation along with that of the pressure perturbation are computed along the spanwise direction and depicted in Figure 4. The results of the grid independence study are given in the next section.

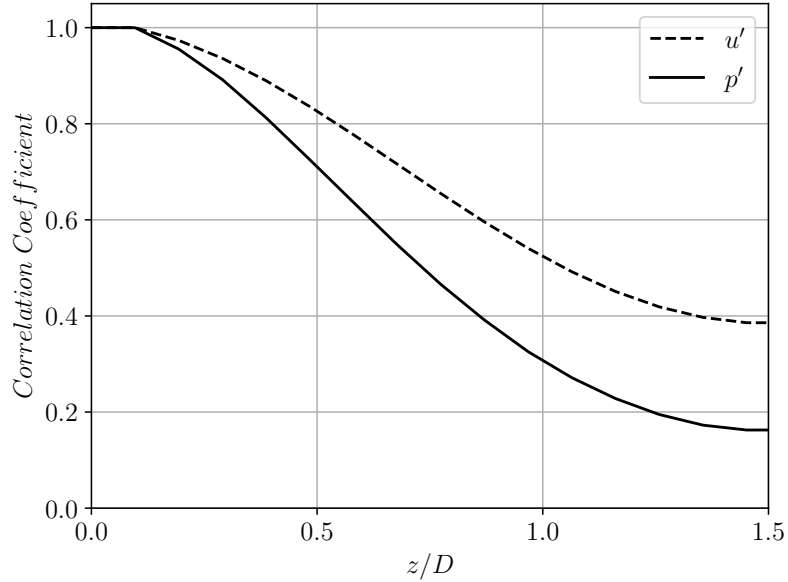


Figure 4. The correlation coefficient in the spanwise direction for the three-dimensional open deep cavity.

Table 1. A summary of grid independence study of the open deep cavity.

Simulation	$\overline{C_D}$	SPL
$\mathcal{P}2$	0.1314	112.12
$\mathcal{P}3$	0.1098	113.13
$\mathcal{P}4$	0.1115	113.34

3.1.2 RESULTS AND DISCUSSION

The grid independence study is performed by increasing the solution polynomial degree, which increases the resolution of the simulation. The time-averaged drag coefficient and the sound pressure level at an observer located $7.16D$ above the center of the cavity are computed using solution polynomial degrees of $\mathcal{P}2$, $\mathcal{P}3$, and $\mathcal{P}4$ to show the grid independency.

The drag coefficient is defined as

$$C_D = \frac{F_x}{\frac{1}{2}\rho_\infty U_\infty^2 DW}, \quad (19)$$

where F_x is the force in the x -direction computed on the three cavity walls, ρ_∞ is the free-stream density, and U_∞ is the free-stream velocity. The time-averaged drag coefficient along with the SPL at the observer, for different simulations, are given in Table 1. 30 observer points along the span of the cavity are used. The time-averaged pressure and root-mean-squared of the pressure perturbation are computed for each observer point and then spatially averaged to find the SPL at the observer location. These results show that the $\mathcal{P}3$ simulation provides sufficient resolution for this study.



Figure 5. The design variable, h_{TE} , for the open deep cavity.

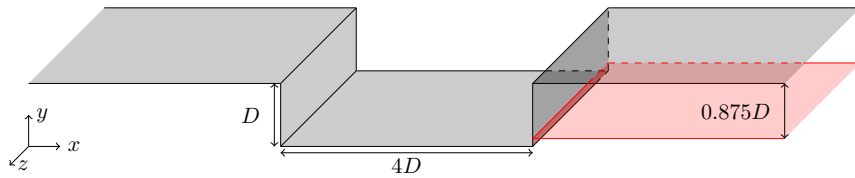


Figure 6. The baseline, in black, and optimum, in red, designs of the open cavity.

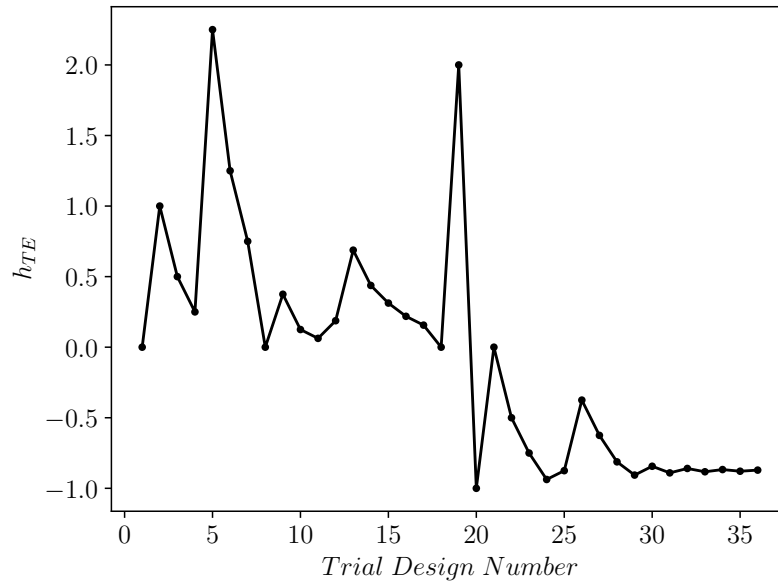
3.2 OPTIMIZATION

In this section, the noise at the observer point located at $\mathbf{x}_{obs}/D = [2, 7.16]$ is minimized by changing the height of the cavity trailing edge wall, h_{TE} , depicted in Figure 5. Thus, $\mathbf{X} = h_{TE}$ is the design variable and $\mathbf{X}_0 = 0$, while the objective function is $\mathcal{F} = p'_{rms}$. Upper and lower bounds of -1 and 4 , respectively, are chosen for the design variable, h_{TE} .

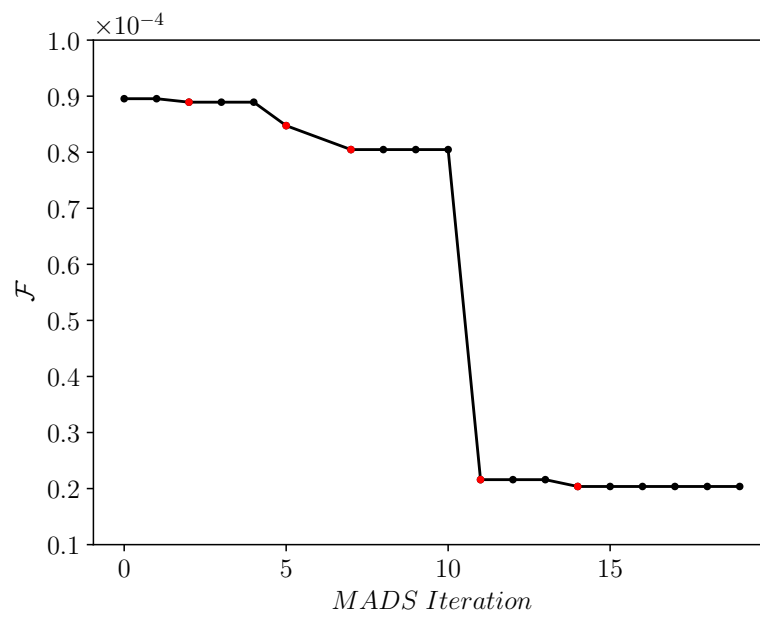
3.2.1 RESULTS AND DISCUSSION

The optimization procedure converged after 19 MADS iterations with a total of 36 objective function evaluations. The optimal design parameter is identified as $h_{TE} = -0.875$, resulting in an SPL of 100.27 dB, signifying a 12.86 dB reduction in noise. The baseline and optimum designs are depicted in Figure 6. Moreover, Figure 7 illustrates the explored design parameter space and the convergence of the objective function.

The Q-criterion contours coloured by velocity magnitude and the pressure perturbation of both the baseline and optimum designs are shown in Figures 8 and 9, respectively. Comparing these figures, turbulent structures over the cavity are reduced significantly in the optimum design, and the shear layer expands over the cavity, resulting in much lower noise emission. Furthermore, the Power Spectral Density (PSD) of the sound pressure level is plotted against the Strouhal number for both the baseline and optimum designs in Figure 10, which follows the Welch's method of periodograms [54] and involves dividing the time period into 6 windows with a 50% overlap. This figure illustrates the SPL reduction across all frequency ranges.



(a) The design space.



(b) The objective function convergence with the new incumbent designs highlighted in red.

Figure 7. The design space and objective function convergence for the three-dimensional open deep cavity.

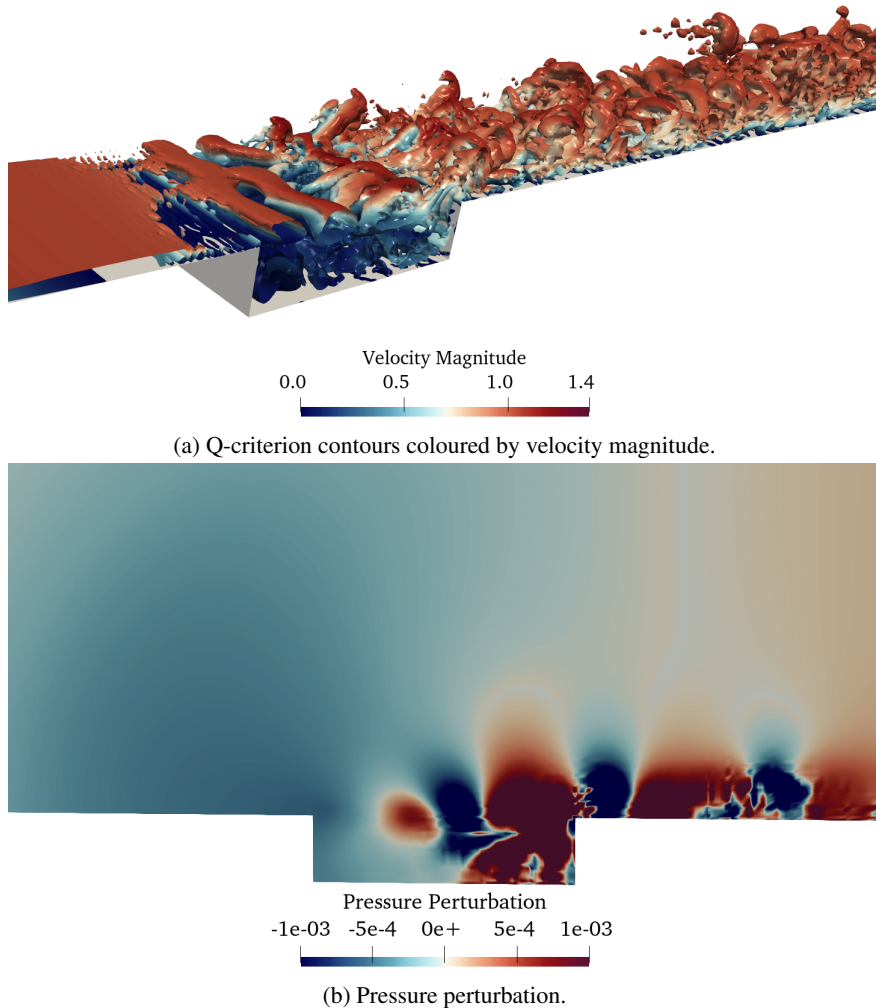


Figure 8. The Q-criterion contours and pressure perturbation for the baseline design of the open deep cavity.

4 TANDEM CYLINDERS

The flow around two tandem cylinders consists of multiple flow features including flow separation, reattachment, recirculation, and quasi-periodic vortex shedding, amongst others. The physics of such flows is highly dependent on the diameter ratio of the cylinders, the spacing between them, and the Reynolds number. The diameter ratio of the cylinders is defined as $r = D_d/D_u$, where D_d and D_u are the downstream and upstream diameter of the cylinders, respectively. The spacing of the cylinders, s , is defined as the distance between the rear of the upstream cylinder to the front of the downstream cylinder. These definitions are depicted in Figure 11.

The three-dimensional wake development of a single cylinder was studied by Williamson [55]. Additionally, Papaioannou et al. [56] investigated the three-dimensionality effects of flow over two tandem cylinders, varying Reynolds number and the spacing distance between the cylinders. They found that as Reynolds number increased, two-dimensional results

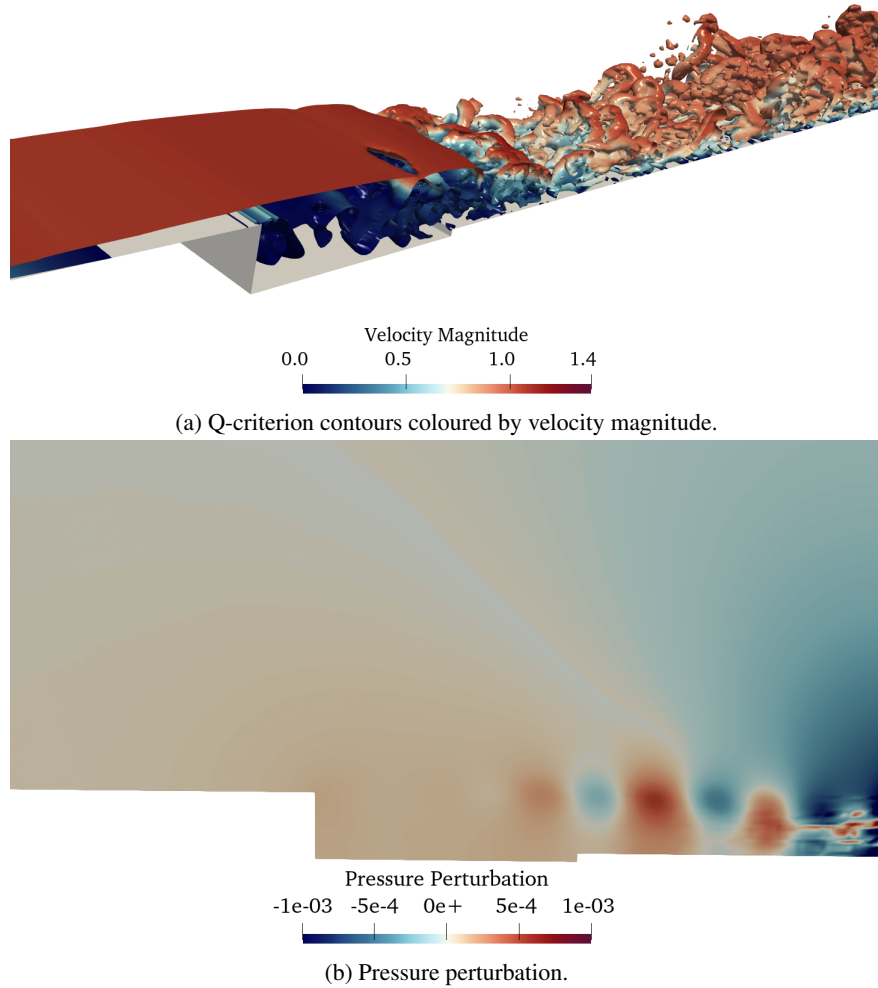


Figure 9. The Q-criterion contours and pressure perturbation for the optimum design of the open deep cavity.

diverged from three-dimensional ones, especially beyond a critical Reynolds number where wake three-dimensionality initiated. The Reynolds number of our study, based on the upstream cylinder's diameter, is $Re_D = 1000$ since the wake will develop considerable three-dimensionality and this Reynolds number is associated with the early turbulent regime [56].

4.1 VALIDATION

In this section, the simulation of flow over two tandem cylinders is validated using reference DNS data [56], along with grid independence study of the time-averaged lift and drag coefficients and SPL at a near-field observer located $2D$ above the upstream cylinder. Then, the optimization is performed similar to our previous work [39], where sound at

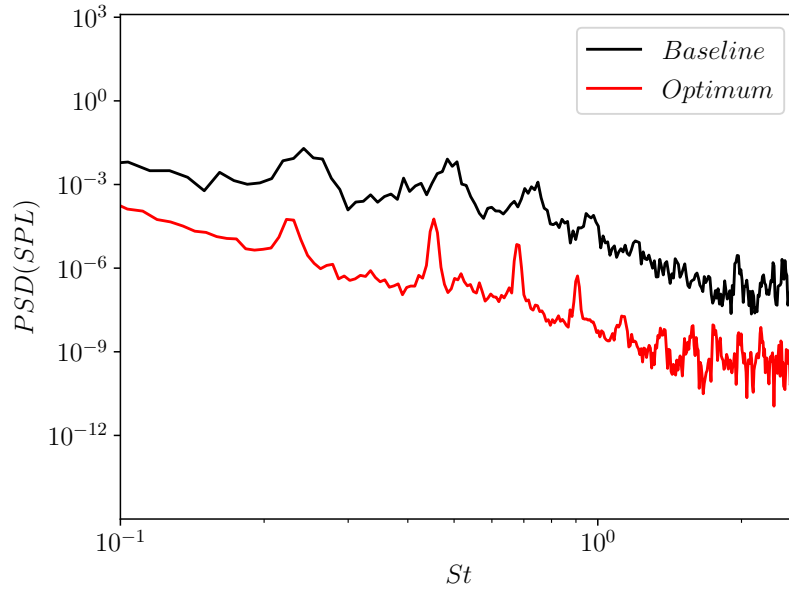


Figure 10. The sound spectra for the open deep cavity.

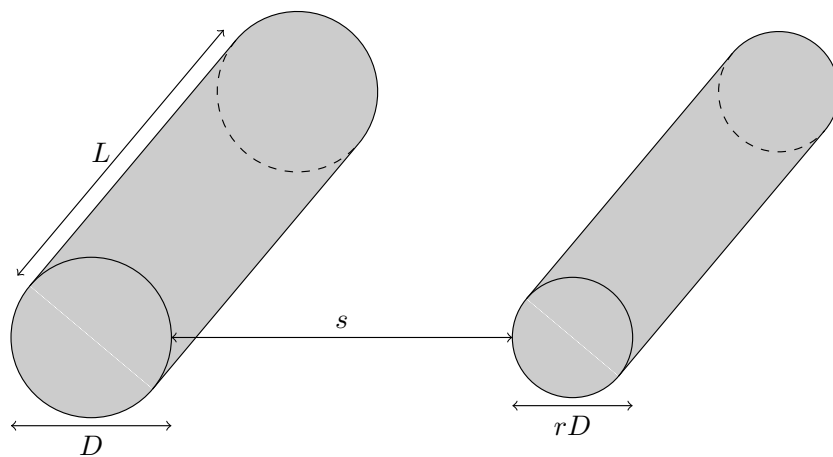


Figure 11. The geometry of two cylinders in a tandem configuration.

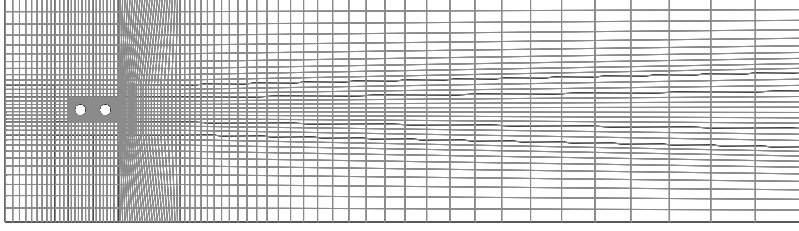


Figure 12. The mesh of the two cylinders in a tandem configuration.

the near-field observer is minimized. The design variables are the ratio of the cylinders' diameters, r , and the distance between the two, s .

4.1.1 COMPUTATIONAL DETAILS

The cylinders are located at a distance of $s/D = 1$ with a ratio of $r = 1$ and have a spanwise length of $L/D = 10$, following previous studies [56]. The Reynolds number, based on the upstream cylinder's diameter, is $Re_D = 1000$, corresponding to the early turbulent regimes [56], and the Mach number is 0.2. The boundary layer region extends to $0.5D$ around the cylinders, with the inlet boundary placed $5D$ away from the upstream cylinder and the outlet boundary $55D$ away from the downstream cylinder. The computational domain is extended to $10D$ in the y -direction. The stretching ratio for the first $5D$ and $1D$ elements in the x and y -directions, respectively, is 1.05, and that of the remaining elements is 1.075. The smallest element size in the domain is $0.1D$, which is in the boundary layer region. A total number of 31,780 hexagonal elements are used. The mesh of the tandem cylinders is shown in Figure 12. Periodic boundary conditions are applied in the spanwise direction, while a no-slip boundary condition is imposed on the surface of the cylinders, along with Riemann invariant boundary conditions at the inlet and outlet of the computational domain. The simulation is run for $100t_c$, where $t_c = D/U_\infty$, to allow initial transients to disappear, followed by a subsequent period of $500t_c$ to obtain an average of the statistical quantities.

4.1.2 RESULTS AND DISCUSSION

The sufficiency of the spanwise length is investigated by computing the correlation coefficient of the velocity fluctuation and the pressure perturbation along the z -direction. The correlation plot, demonstrated in Figure 13, ensures the uncorrelated fluctuations in the z -direction at a separation of half of the domain size. Furthermore, the time-averaged drag coefficient and the sound pressure level at the observer are computed using different averaging window lengths, summarized in Table 2. The time-averaged drag coefficient of the upstream cylinder is computed using $\mathcal{P}2$ and $\mathcal{P}3$ simulations. The $\overline{C_{D1}}$ obtained using the $\mathcal{P}3$ simulation is 0.997, which is in good agreement with the reference value of 0.988 [56]. Table 2 shows that the difference in the statistical time-averaged quantities is negligible beyond $500t_c$. Thus, in this study, the statistical quantities are averaged for $500t_c$.

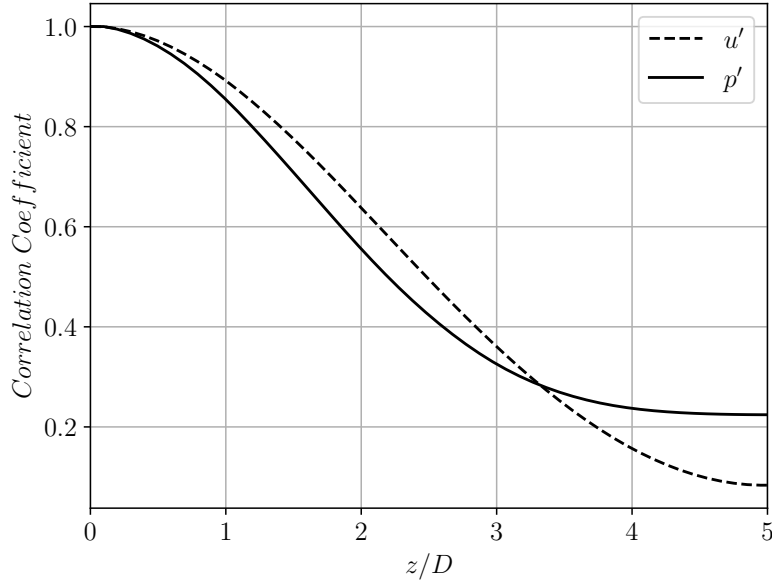


Figure 13. The correlation coefficient in the spanwise direction for the tandem cylinders.

Table 2. The $\overline{C_{D1}}$ and SPL at the observer, for the tandem cylinders configuration using different lengths of the averaging window.

Averaging Window Size	$\overline{C_{D1}}$		SPL	
	$\mathcal{P}2$	$\mathcal{P}3$	$\mathcal{P}2$	$\mathcal{P}3$
$200t_c$	0.962374	0.994465	126.49	125.14
$300t_c$	0.963871	0.994915	126.87	125.23
$400t_c$	0.965569	0.996092	127.34	125.25
$500t_c$	0.966651	0.996752	127.56	125.25
$600t_c$	0.967519	0.997042	127.73	125.31
$700t_c$	0.968142	0.996965	127.84	125.30

4.2 OPTIMIZATION

The distance between the two cylinders, s , and the ratio between the diameters of the cylinders, r , are the design variables, $\mathbf{X} = [s, r]$. The objective function is $\mathcal{F} = p'_{rms}$ at $2D$ above the upstream cylinder.

4.2.1 RESULTS AND DISCUSSION

The optimization problem converges in 18 MADS iterations with a total of 48 objective function evaluations. The baseline and optimum designs are shown in Figure 14. The design space and objective function convergence are shown in Figure 15, where the optimum design is found as $(s, r) = (2.0291D, 1.7563D)$. The optimization process explores a wide range of design variables, as illustrated in Figure 15a. Q-criterion contours, coloured by velocity magnitude, and acoustic field at the mid-plane are shown for both the baseline and optimum designs in Figures 16 and 17, respectively. The optimized design exhibits a smoother flow field, resulting in reduced noise emissions. The SPL of the initial design at the observer, $2D$ above the upstream cylinder, is 125.30 dB , which decreases to 114.10 dB for the optimized

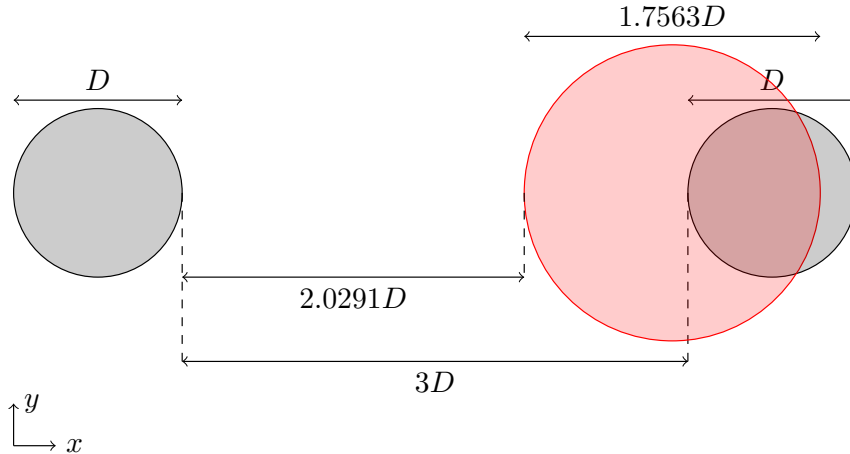


Figure 14. The baseline, in black, and optimum, in red, designs of the tandem cylinders.

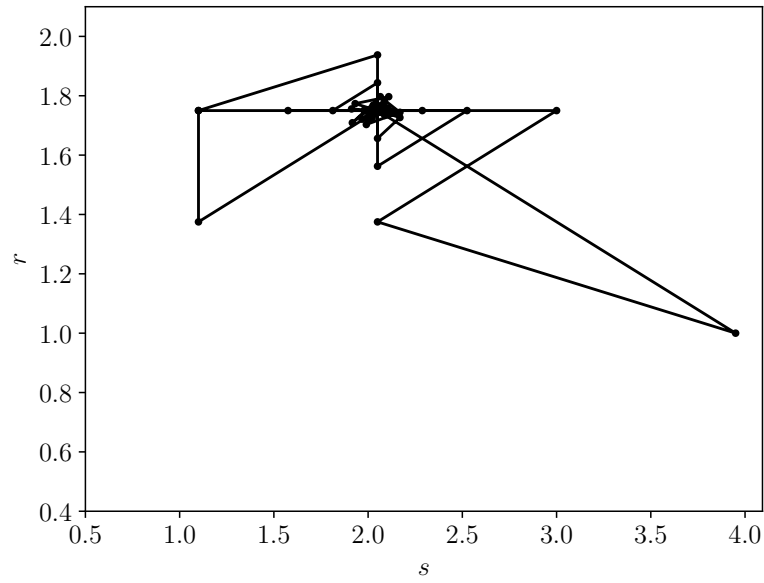
configuration. Lastly, Figure 18 presents the PSD of SPL versus Strouhal number, computed using Welch’s method of periodograms [54] with 3 windows and a 50% overlap. It is evident that the optimum design displays higher intensity PSD of SPL over a broad frequency range, while achieving a lower SPL value. This behavior can be attributed to the baseline design producing high-intensity sound at specific frequencies ($St = 0.63, 0.77, \text{ and } 0.90$), contributing to its elevated peak SPL, whereas the optimum design distributes its energy across a wider frequency spectrum.

5 NACA 4-DIGIT AIRFOIL

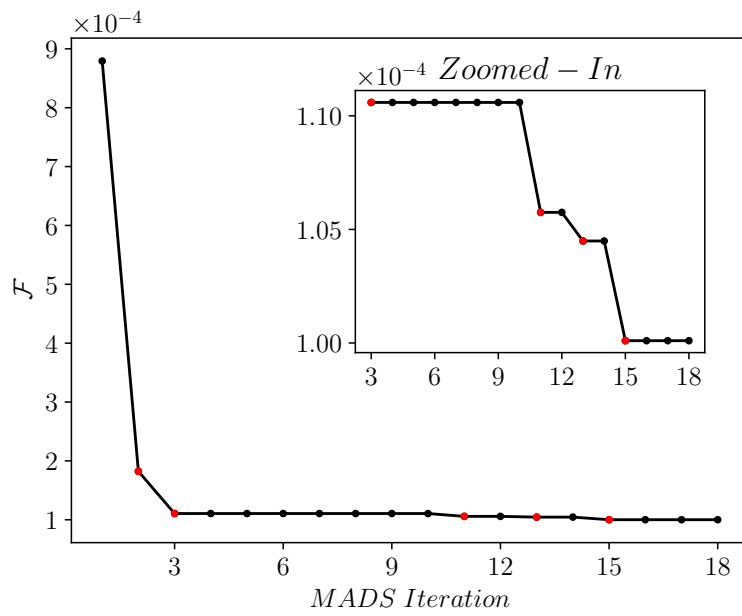
The flow over NACA 4-digit airfoils is investigated in this section. The computational domain, previously used by the authors [39], is extruded in the z -direction. The validation of the flow simulation is conducted using an ILES reference [57] and a grid independence study for a NACA0012 airfoil. Subsequently, four design parameters, akin to those in [39], are selected, and the gradient-free MADS optimization technique is employed. The maximal positive basis construction is employed for the optimization algorithm.

5.1 VALIDATION

Validation for flow over a NACA0012 airfoil at an angle of attack of 6° is conducted. The validation process involves comparing the time-averaged lift and drag coefficients obtained from two distinct grid resolutions with those from an ILES reference [57]. Moreover, the SPL at a near-field observer is computed using both grid resolutions and various time averaging window lengths. This analysis ensures the independence of the results to both grid resolution and time averaging window lengths. Detailed computational procedures and validation results are presented in the subsequent sections.



(a) The design space.



(b) The objective function convergence with the new incumbent designs highlighted in red.

Figure 15. The design space and objective function convergence for the tandem cylinders.

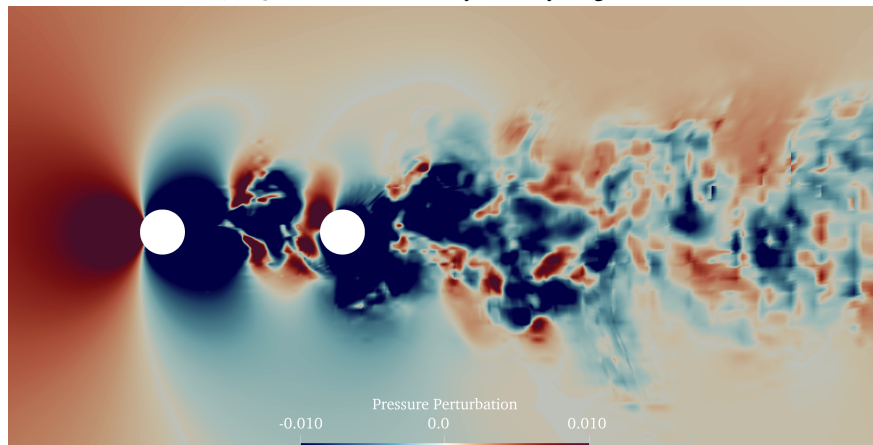
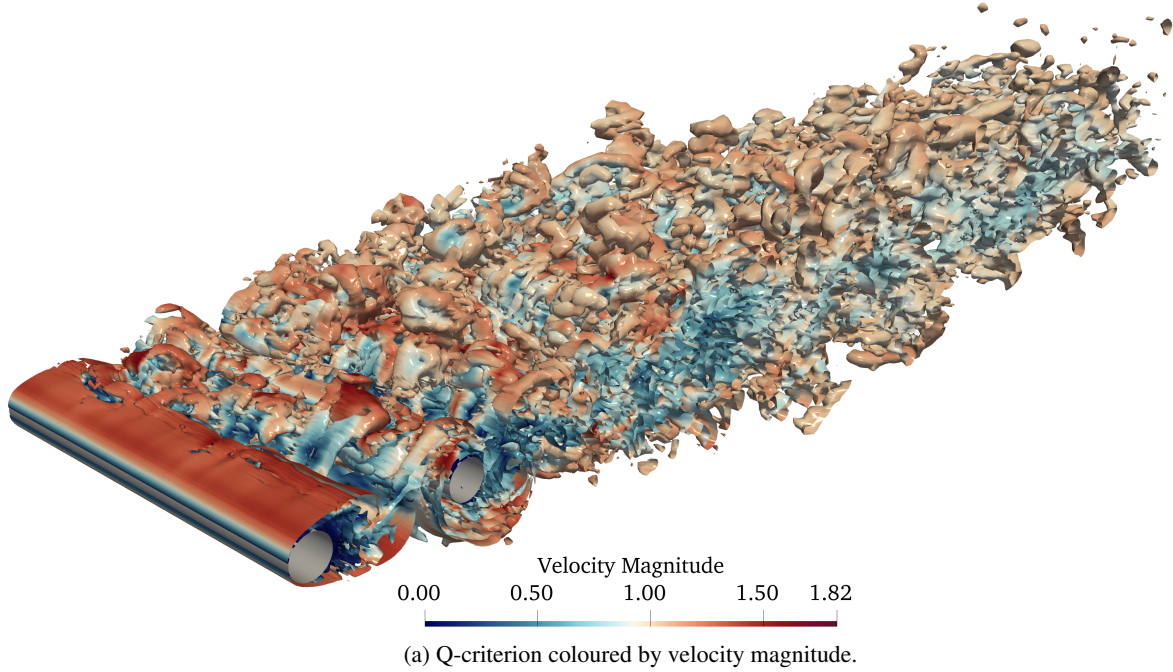
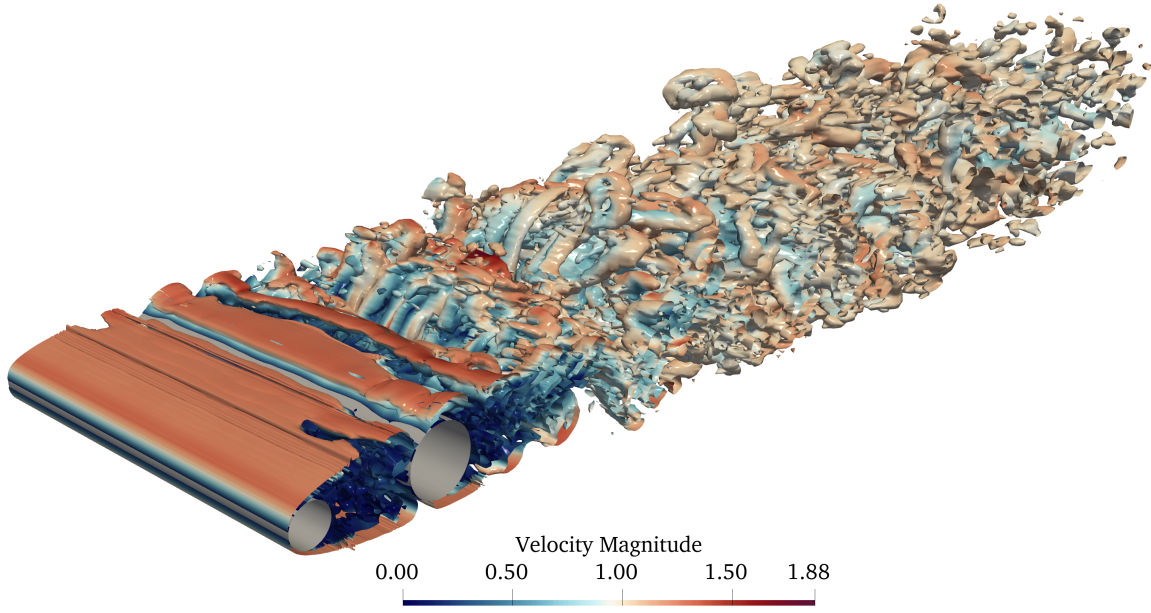


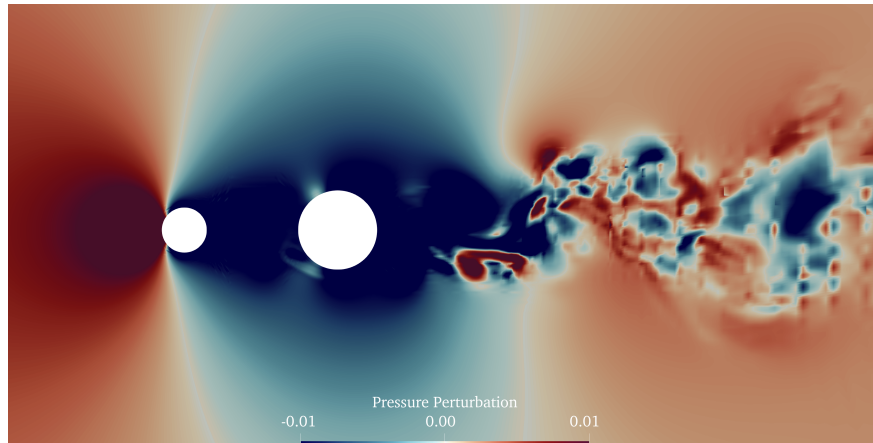
Figure 16. The baseline tandem cylinder design at $t_c = 600$.

5.1.1 COMPUTATIONAL DETAILS

The computational grid consists of 121,520 hexagonal elements, illustrated in Figure 19. The domain extends to $20c$ in the x -direction, $10c$ in the y -direction, and $0.2c$ in the z -direction, with $c = 1$ representing the airfoil chord. Notably, elements in the wake region are inclined at the angle of attack to accurately capture trailing-edge vortices. The flow conditions are characterized by a Reynolds number of 23,000, a free-stream Mach number of $M = 0.2$, and Prandtl number is $Pr = 0.71$. The simulation is run for 10 convective times to allow the initial transition disappears and then run for another 90 convective times for flow statistics averaging. Additionally, a variable solution polynomial degree is implemented to eliminate acoustic wave reflections from boundaries, as demonstrated in Figure 20.



(a) Q-criterion coloured by velocity magnitude.



(b) Acoustic pressure field at mid-plane.

Figure 17. The optimum tandem cylinder design at $t_c = 600$.

5.1.2 RESULTS AND DISCUSSION

Two distinct grid resolutions are employed with maximum solution polynomial degrees of $\mathcal{P}3$ and $\mathcal{P}4$. The time-averaged lift and drag coefficients are compared to the ILES reference data [57], presented in Table 3. The difference between the time-averaged lift coefficient obtained from the $\mathcal{P}4$ simulation and the reference data is minimal, affirming the adequacy of the $\mathcal{P}4$ simulation's grid resolution. Furthermore, the time-averaged drag coefficient differs by less than 1.3% from the reference data. The SPL at an observer located two unit chord lengths below the trailing edge is computed for both $\mathcal{P}3$ and $\mathcal{P}4$ simulations. Various averaging window lengths are applied, and the results are summarized in Table 4. Considering the findings presented in Tables 3 and 4, we opt to conduct $\mathcal{P}4$ simulation for a total duration of 70 convective times for the optimization study.

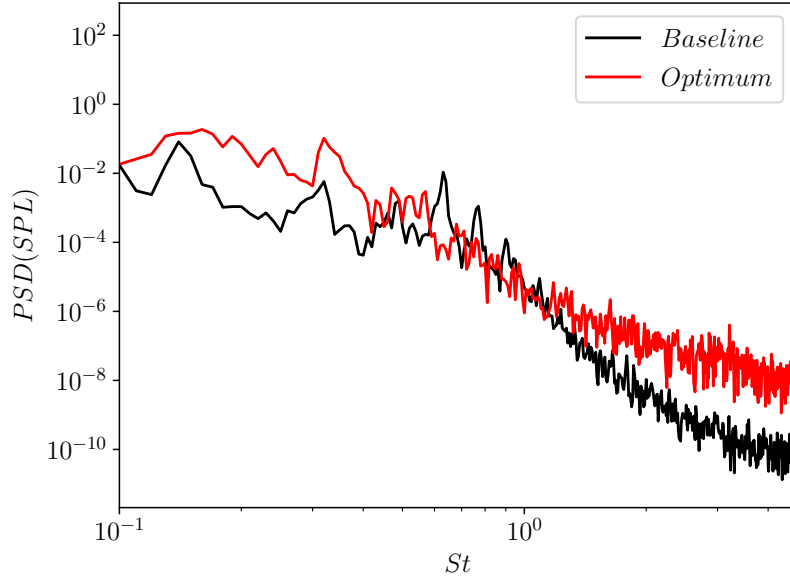
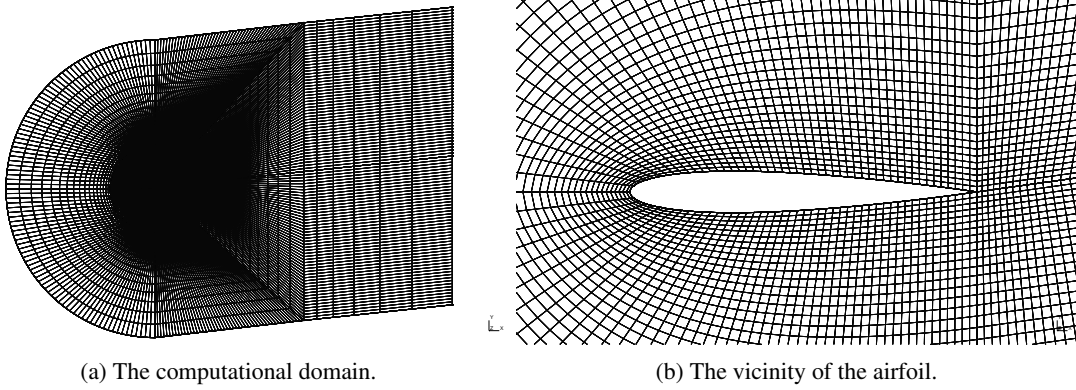


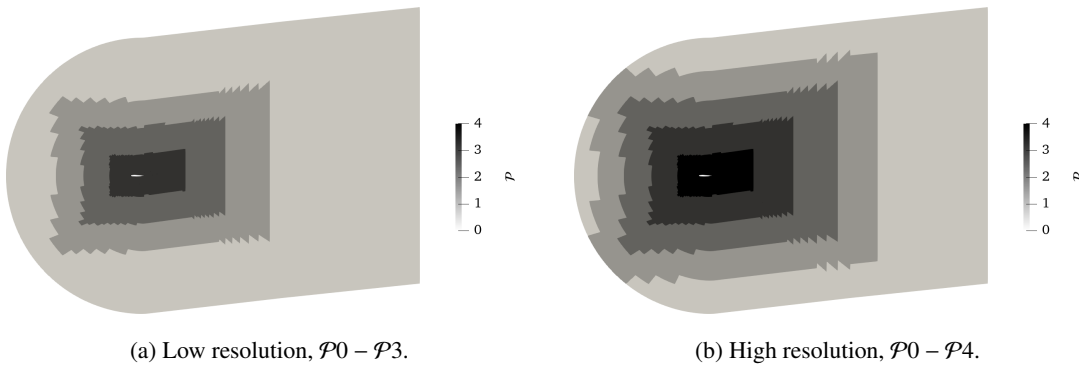
Figure 18. The sound spectra for the tandem cylinders.



(a) The computational domain.

(b) The vicinity of the airfoil.

Figure 19. The computational grid for NACA0012 airfoil at $\alpha = 6^\circ$.



(a) Low resolution, $\mathcal{P}0 - \mathcal{P}3$.

(b) High resolution, $\mathcal{P}0 - \mathcal{P}4$.

Figure 20. Different solution polynomial distributions for grid independence study of NACA0012 airfoil at $\alpha = 6^\circ$.

Table 3. The time-averaged lift and drag coefficients of NACA0012 airfoil at $\alpha = 6^\circ$.

	$\mathcal{P}0 - \mathcal{P}3$	$\mathcal{P}0 - \mathcal{P}4$	reference [57]
$\overline{C_L}$	0.6534	0.6399	0.6402
$\overline{C_D}$	0.0553	0.0548	0.0541

Table 4. The grid independence study of SPL using different averaging window lengths for NACA0012 airfoil at $\alpha = 6^\circ$.

Averaging Window Length	SPL in dB	
	$\mathcal{P}0 - \mathcal{P}3$	$\mathcal{P}0 - \mathcal{P}4$
$20t_c$	114.90	116.34
$40t_c$	115.67	116.31
$60t_c$	115.72	116.23
$80t_c$	115.70	116.24

5.2 OPTIMIZATION

The design parameters are maximum camber c_{max}^a and its location $x_{c_{max}^a}$, maximum thickness t_{max}^a , and angle of attack α , i.e. $\mathcal{X} = [c_{max}^a, x_{c_{max}^a}, t_{max}^a, \alpha]$. The maximum camber range is set to $c_{max}^a \in [-10, 10]$ as a percentage of the chord, with the distance from the airfoil leading edge in the range of $x_{c_{max}^a} \in [4, 9]$ as a tenth of the chord. The maximum thickness of the airfoil is within the range of $t_{max}^a \in [6, 18]$ as a percentage of the chord. Finally, the angle of attack varies from 0° to 12° . The objective function is defined as the sound pressure level at the observer with constraints on both the mean lift and mean drag coefficients. A quadratic penalty term is added to the objective function when the lift coefficient deviates from the baseline design, and an additional quadratic penalty term is added when the mean drag coefficient is above the baseline design. The objective function is defined as

$$\mathcal{F} = \begin{cases} SPL + \epsilon_1 (\overline{C_L} - \overline{C_{L,baseline}})^2 + \epsilon_2 (\overline{C_D} - \overline{C_{D,baseline}})^2 & \overline{C_D} > \overline{C_{D,baseline}} \\ SPL + \epsilon_1 (\overline{C_L} - \overline{C_{L,baseline}})^2 & \overline{C_D} \leq \overline{C_{D,baseline}} \end{cases}, \quad (20)$$

where the constants ϵ_1 and ϵ_2 are set to 8,000 and 400,000, respectively, to compensate for the order of magnitude difference in SPL and $\overline{C_L}$ and $\overline{C_D}$. The defined objective function minimizes the sound pressure level while maintaining the mean lift coefficient, and ensures the optimized airfoil has a similar or lower mean drag coefficient.

5.2.1 RESULTS AND DISCUSSION

This optimization procedure converges after 22 MADS iterations, consisting of 172 objective function evaluations. The baseline and optimum designs are shown in Figure 21. The design space and the convergence of the objective function are shown in Figure 22. The optimal airfoil design has a maximum camber of $c_{max}^a = 0.140625$ percent of the chord, at a 6.5 tenth of the chord distance from the leading edge, with a thickness of $t_{max}^a = 8.859375$ percent of the chord, at an angle of attack of $\alpha = 6.28125$ degrees. The SPL of the optimized airfoil is decreased to 110.57 dB, the mean lift coefficient is $\overline{C_L} = 0.6556$, and finally, the mean drag coefficient is decreased by 7.4% to $\overline{C_D} = 0.0509$.

Figures 23 and 24 display the Q-criterion colored by velocity magnitude and the pressure perturbation at mid-planes for the baseline and optimum designs, respectively. The optimal design minimizes large turbulent structures, resulting

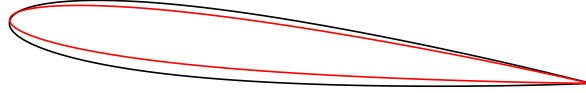


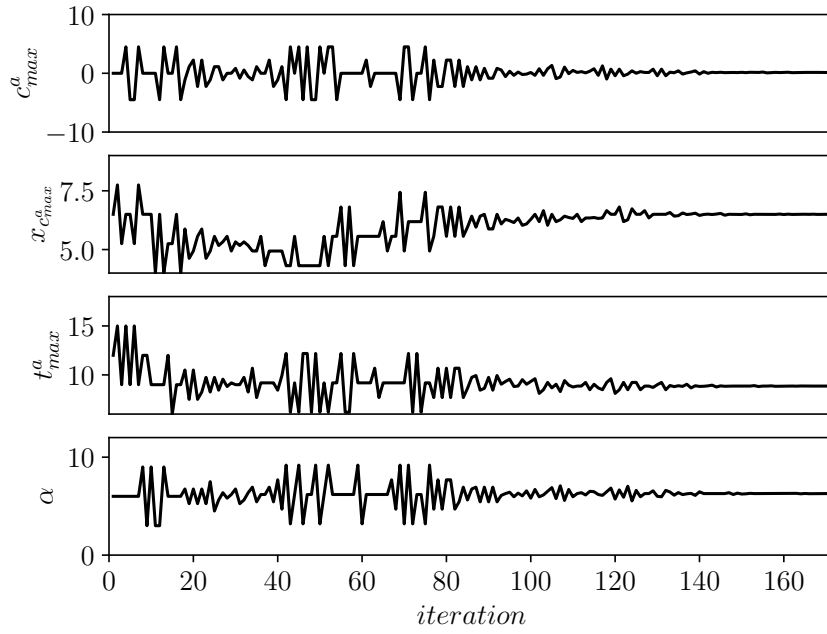
Figure 21. The baseline, in black, and optimum, in red, designs of the NACA 4-digits airfoil.

in a significantly reduced pressure perturbation field and approximately a $5.66dB$ noise reduction. Figure 25 presents the PSD of SPL as a function of the Strouhal number, computed using Welch’s method of periodograms [54] with 3 windows and a 50% overlap. It is evident that the optimum design displays lower-intensity SPL energy across various frequency ranges.

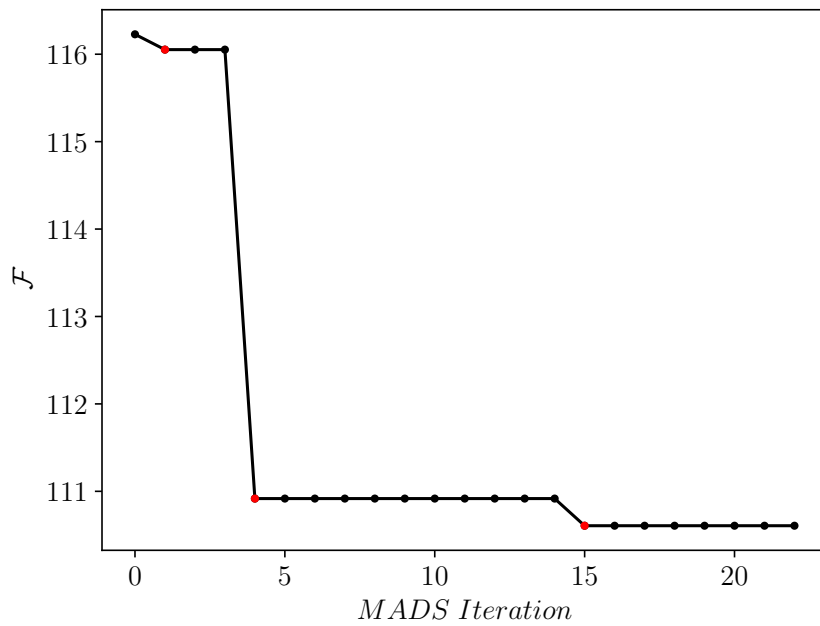
6 CONCLUSIONS

In conclusion, we present an aeroacoustic shape optimization framework using the MADS optimization algorithm in conjunction with high-order FR spatial discretization and LES. Our framework effectively reduces SPL at a near-field observer. Importantly, this research eliminates the runtime dependency on the number of design parameters. Through parallel implementation, we maintain a consistent runtime for each optimization iteration, equivalent to a single CFD simulation, provided adequate computational resources. This addresses a key challenge in gradient-free optimization techniques, enhancing the robustness and computational efficiency of our framework. These findings hold significant importance for aeroacoustic shape optimization, with potential applications in the aerospace industry where noise reduction is of paramount importance.

The feasibility of the proposed aeroacoustic shape optimization framework can be assessed through testing at higher Reynolds numbers and addressing industry-relevant problems. Additionally, exploring the integration of a far-field acoustic solver into the framework is a promising avenue, potentially broadening its capability to address a more extensive range of aeroacoustic challenges. This research suggests the potential for more efficient aeroacoustic shape optimization methods, with notable implications for quieter and more efficient aerodynamic designs.

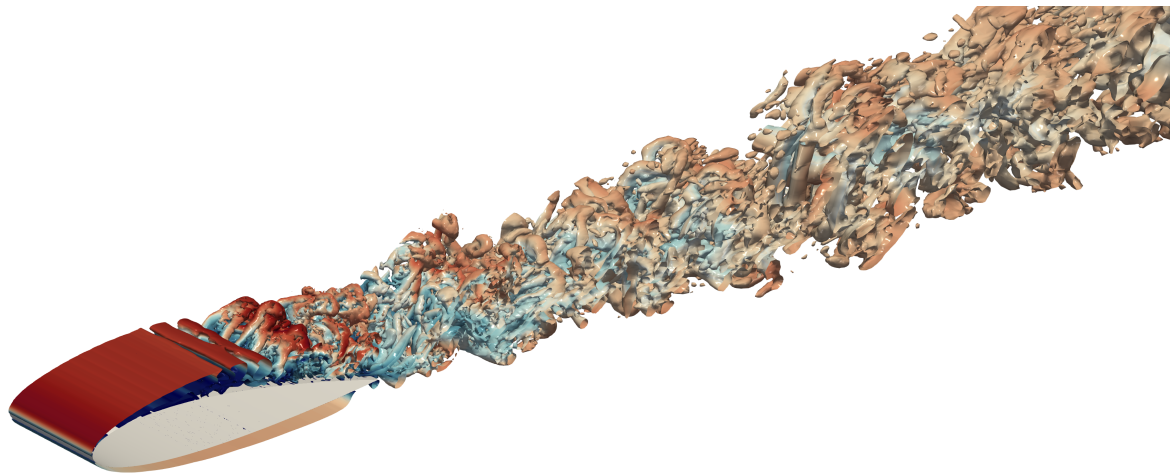


(a) The design space.

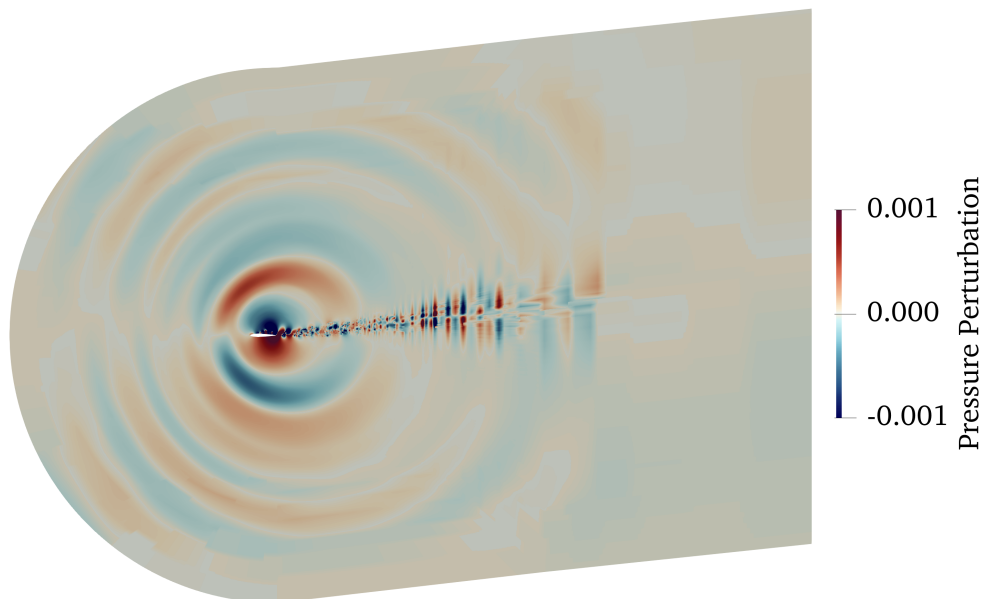


(b) The objective function convergence with the new incumbent design highlighted in red.

Figure 22. The design space and objective function convergence of the NACA 4-digit airfoil optimization.

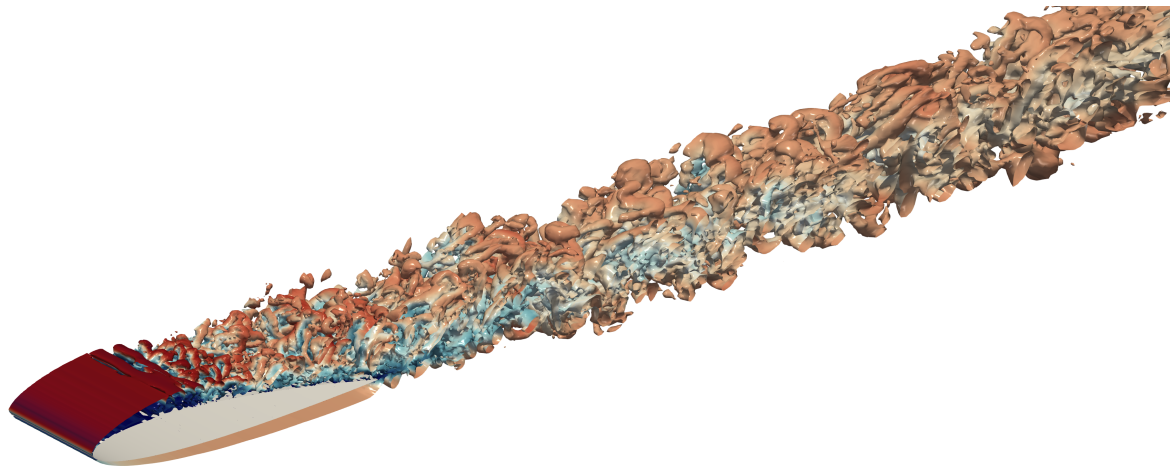


(a) Q-criterion coloured by velocity magnitude.

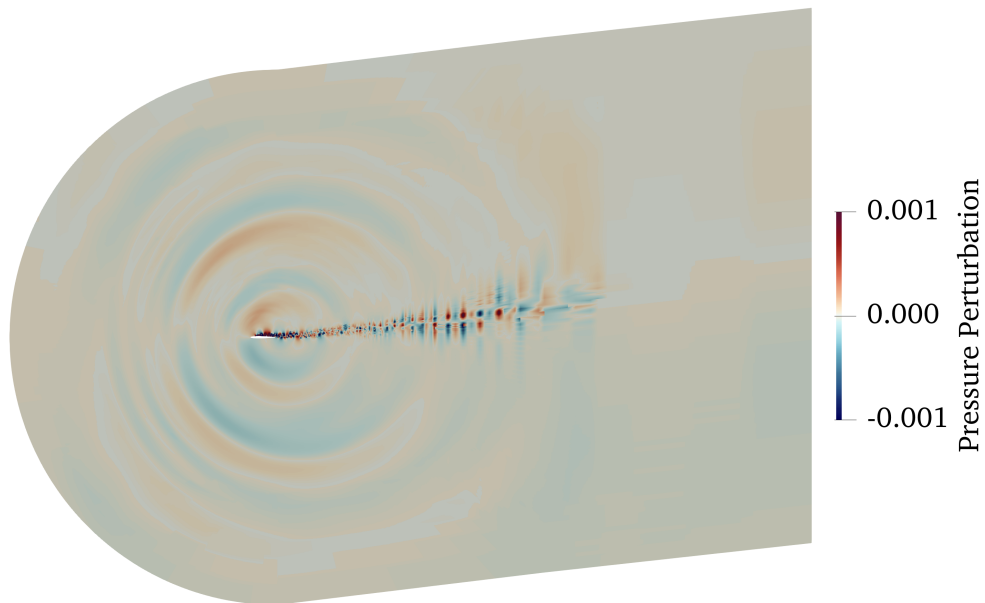


(b) Acoustic pressure field at mid-plane.

Figure 23. The baseline airfoil at $t_c = 70$.



(a) Q-criterion coloured by velocity magnitude.



(b) Acoustic pressure field at mid-plane.

Figure 24. The optimum airfoil at $t_c = 70$.

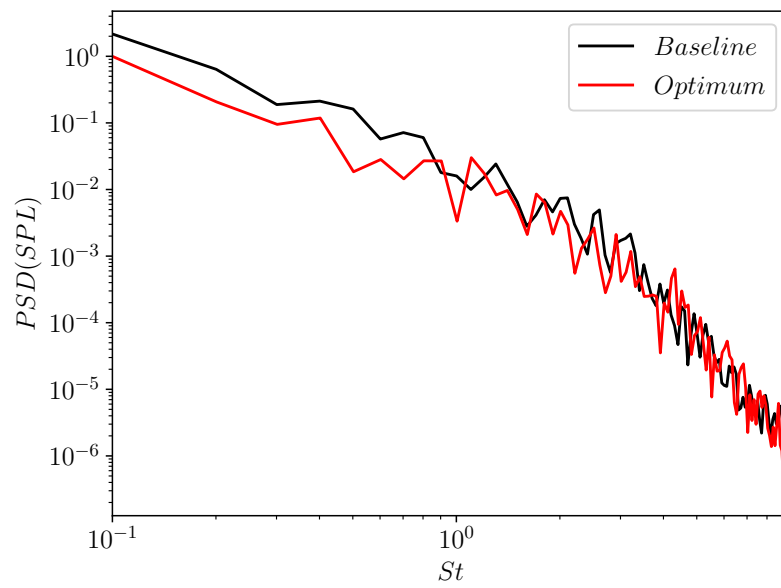


Figure 25. The sound spectra for the NACA 4-digit airfoils.

DATA STATEMENT

Data relating to the results in this manuscript can be downloaded from the publication's website under a CC-BY-NC-ND 4.0 license.

CREDiT AUTHORSHIP CONTRIBUTION STATEMENT

Mohsen Hamedi: Conceptualization; Data curation; Formal analysis; Investigation; Methodology; Software; Validation; Visualization; Writing - original draft. **Brian Vermeire:** Conceptualization; Funding acquisition; Investigation; Methodology; Project administration; Resources; Software; Supervision; Writing - review & editing.

DECLARATION OF COMPETING INTEREST

The authors declare that they have no known competing financial interests or personal relationships that could have appeared to influence the work reported in this paper.

ACKNOWLEDGEMENTS

The authors acknowledge support from the Natural Sciences and Engineering Research Council of Canada (NSERC) [RGPIN-2017-06773] and the Fonds de recherche du Québec (FRQNT) via the nouveaux chercheurs program. This research was enabled in part by support provided by Calcul Québec (www.calculquebec.ca) and the Digital Research Alliance of Canada (www.alliancecan.ca) via a Resources for Research Groups allocation. M.H acknowledges Fonds de Recherche du Québec - Nature et Technologie (FRQNT) via a B2X scholarship.

REFERENCES

- [1] World Health Organization et al. *Burden of Disease from Environmental Noise: Quantification of Healthy Life Years Lost in Europe*. World Health Organization. Regional Office for Europe, 2011.
- [2] A. Mahashabde, P. Wolfe, A. Ashok, C. Dorbian, Q. He, A. Fan, S. Lukachko, A. Mozdzanowska, C. Wollersheim, S. R. H. Barrett, et al. Assessing the environmental impacts of aircraft noise and emissions. *Progress in Aerospace Sciences*, 47(1):15–52, 2011.
- [3] M. Basner, C. Clark, A. Hansell, J. I. Hileman, S. Janssen, K. Shepherd, and V. Sparrow. Aviation noise impacts: state of the science. *Noise & Health*, 19(87):41, 2017.
- [4] C. B. Pepper, M. A. Nascarella, and R. J. Kendall. A review of the effects of aircraft noise on wildlife and humans, current control mechanisms, and the need for further study. *Environmental Management*, 32:418–432, 2003.

- [5] J. Kou, L. Botero-Bolívar, R. Ballano, O. Marino, L. de Santana, E. Valero, and E. Ferrer. Aeroacoustic airfoil shape optimization enhanced by autoencoders. *Expert Systems with Applications*, 217:119513, 2023.
- [6] K. Volkmer and T. Carolus. Aeroacoustic airfoil shape optimization utilizing semi-empirical models for trailing edge noise prediction. In *2018 AIAA/CEAS Aeroacoustics Conference*, page 3130, 2018.
- [7] B. R. Jones, W. A. Crossley, and A. S. Lyrintzis. Aerodynamic and aeroacoustic optimization of rotorcraft airfoils via a parallel genetic algorithm. *Journal of Aircraft*, 37(6):1088–1096, 2000.
- [8] W. Klimczyk and A. Sieradzki. RANS-based aeroacoustic global sensitivity study and optimization of UAV propellers. *Aerospace*, 10(3):306, 2023.
- [9] M. Monfaredi, X. S. Trompoukis, K. T. Tsiakas, and K. C. Giannakoglou. An unsteady aerodynamic/aeroacoustic optimization framework using continuous adjoint. *Advances in Evolutionary and Deterministic Methods for Design, Optimization and Control in Engineering and Sciences*, pages 147–162, 2021.
- [10] M. Monfaredi, X. Trompoukis, K. Tsiakas, and K. Giannakoglou. Unsteady continuous adjoint to URANS coupled with FW-H analogy for aeroacoustic shape optimization. *Computers & Fluids*, 230:105136, 2021.
- [11] N. Ricks, P. Tsirikoglou, F. Contino, and G. Ghorbaniasl. A CFD-based methodology for aerodynamic-aeroacoustic shape optimization of airfoils. In *AIAA Scitech 2020 Forum*, page 1729, 2020.
- [12] B. Yuepeng, S. Wenping, H. Zhonghua, Y. Zhang, and L. Zhang. Aerodynamic/aeroacoustic variable-fidelity optimization of helicopter rotor based on hierarchical Kriging model. *Chinese Journal of Aeronautics*, 33(2):476–492, 2020.
- [13] J. Slotnick, A. Khodadoust, J. Alonso, D. Darmofal, W. Gropp, E. Lurie, and D. Mavriplis. CFD vision 2030 study: A path to revolutionary computational aerosciences. 2014.
- [14] T. Colonius and S. K. Lele. Computational aeroacoustics: progress on nonlinear problems of sound generation. *Progress in Aerospace Sciences*, 40(6):345–416, 2004.
- [15] A. L. Marsden, M. Wang, J. E. Dennis, and P. Moin. Trailing-edge noise reduction using derivative-free optimization and large-eddy simulation. *Journal of Fluid Mechanics*, 572:13–36, 2007.
- [16] A. L. Marsden, M. Wang, B. Mohammadi, and P. Moin. Shape optimization for aerodynamic noise control. *Center for Turbulence Research Annual Brief*, pages 241–47, 2001.
- [17] OpenFOAM. <http://www.openfoam.org>. [online].
- [18] SU2. <http://su2.stanford.edu>. [online].
- [19] F. Palacios, J. Alonso, K. Duraisamy, M. Colonno, J. Hicken, A. Aranake, A. Campos, S. Copeland, T. Economon, A. Lonkar, et al. Stanford university unstructured (SU2): an open-source integrated computational environment for multi-physics simulation and design. In *51st AIAA Aerospace Sciences Meeting Including the New Horizons Forum and Aerospace Exposition*, page 287, 2013.
- [20] CHARLES. <http://www.cascadetechnologies.com/charles>. [online].

- [21] Stanford Researchers Break Million-Core Supercomputer Barrier. <http://engineering.stanford.edu/news/stanford-researchers-break-million-core-supercomputer-barrier>. [online].
- [22] P. Vincent, F. Witherden, B. Vermeire, J. S. Park, and A. Iyer. Towards green aviation with python at petascale. In *SC'16: Proceedings of the International Conference for High Performance Computing, Networking, Storage and Analysis*, pages 1–11. IEEE, 2016.
- [23] J. Langguth, N. Wu, J. Chai, and X. Cai. On the GPU performance of cell-centered finite volume method over unstructured tetrahedral meshes. In *Proceedings of the 3rd Workshop on Irregular Applications: Architectures and Algorithms*, pages 1–8, 2013.
- [24] H. T. Huynh. A flux reconstruction approach to high-order schemes including discontinuous Galerkin methods. In *18th AIAA Computational Fluid Dynamics Conference*, page 4079, 2007.
- [25] B. C. Vermeire, S. Nadarajah, and P. G. Tucker. Implicit large eddy simulation using the high-order correction procedure via reconstruction scheme. *International Journal for Numerical Methods in Fluids*, 82(5):231–260, 2016.
- [26] M. Hamed and B. C. Vermeire. Optimized filters for stabilizing high-order large eddy simulation. *Computers & Fluids*, 237:105301, 2022.
- [27] R. Abgrall and M. Ricchiuto. High order methods for CFD, 2017.
- [28] J. S. Hesthaven. *Numerical Methods for Conservation Laws: From Analysis to Algorithms*. SIAM, 2017.
- [29] Z. J. Wang, K. Fidkowski, R. Abgrall, F. Bassi, D. Caraeni, A. Cary, H. Deconinck, R. Hartmann, K. Hillewaert, H. T. Huynh, et al. High-order CFD methods: current status and perspective. *International Journal for Numerical Methods in Fluids*, 72(8):811–845, 2013.
- [30] O. Pironneau. On optimum design in fluid mechanics. *Journal of Fluid Mechanics*, 64(1):97–110, 1974.
- [31] A. Jameson. Aerodynamic design via control theory. *Journal of Scientific Computing*, 3:233–260, 1988.
- [32] Z. Lyu and J. R. R. A. Martins. Aerodynamic design optimization studies of a blended-wing-body aircraft. *Journal of Aircraft*, 51(5):1604–1617, 2014.
- [33] B. Y. Zhou, T. A. Albring, N. R. Gauger, T. D. Economou, F. Palacios, and J. J. Alonso. A discrete adjoint framework for unsteady aerodynamic and aeroacoustic optimization. In *16th AIAA/ISSMO Multidisciplinary Analysis and Optimization Conference*, page 3355, 2015.
- [34] H. R. Karbasian and B. C. Vermeire. Sensitivity analysis of chaotic dynamical systems using a physics-constrained data-driven approach. *Physics of Fluids*, 34(1), 2022.
- [35] C. Audet and J. E. Dennis Jr. Mesh adaptive direct search algorithms for constrained optimization. *SIAM Journal on Optimization*, 17(1):188–217, 2006.
- [36] M. A. Abramson, C. Audet, J. E. Dennis Jr, and S. L. Digabel. OrthoMADS: A deterministic MADS instance with orthogonal directions. *SIAM Journal on Optimization*, 20(2):948–966, 2009.

- [37] H. R. Karbasian and B. C. Vermeire. Gradient-free aerodynamic shape optimization using large eddy simulation. *Computers & Fluids*, 232:105185, 2022.
- [38] A. Aubry, H. R. Karbasian, and B. C. Vermeire. High-fidelity gradient-free optimization of low-pressure turbine cascades. *Computers & Fluids*, 248:105668, 2022.
- [39] M. Hamedi and B. Vermeire. Near-field aeroacoustic shape optimization at low Reynolds numbers. *arXiv preprint arXiv:2310.10574*, 2023.
- [40] S. Hedayati Nasab, C. A. Pereira, and B. C. Vermeire. Optimal Runge-Kutta stability polynomials for multidimensional high-order methods. *Journal of Scientific Computing*, 89(1):11, 2021.
- [41] B. C. Vermeire, N. A. Loppi, and P. E. Vincent. Optimal embedded pair Runge-Kutta schemes for pseudo-time stepping. *Journal of Computational Physics*, 415:109499, 2020.
- [42] Z. J. Wang and H. Gao. A unifying lifting collocation penalty formulation including the discontinuous Galerkin, spectral volume/difference methods for conservation laws on mixed grids. *Journal of Computational Physics*, 228(21):8161–8186, 2009.
- [43] B. C. Vermeire, F. D. Witherden, and P. E. Vincent. On the utility of GPU accelerated high-order methods for unsteady flow simulations: A comparison with industry-standard tools. *Journal of Computational Physics*, 334:497–521, 2017.
- [44] V. Torczon. On the convergence of pattern search algorithms. *SIAM Journal on Optimization*, 7(1):1–25, 1997.
- [45] I. D. Coope and C. J. Price. On the convergence of grid-based methods for unconstrained optimization. *SIAM Journal on Optimization*, 11(4):859–869, 2001.
- [46] C. Davis. Theory of positive linear dependence. *American Journal of Mathematics*, 76(4):733–746, 1954.
- [47] D. J. Maull and L. F. East. Three-dimensional flow in cavities. *Journal of Fluid Mechanics*, 16(4):620–632, 1963.
- [48] D. Rockwell and C. Knisely. Observations of the three-dimensional nature of unstable flow past a cavity. *The Physics of Fluids*, 23(3):425–431, 1980.
- [49] S. J. Lawson and G. N. Barakos. Review of numerical simulations for high-speed, turbulent cavity flows. *Progress in Aerospace Sciences*, 47(3):186–216, 2011.
- [50] X. Gloerfelt, C. Bogey, and C. Bailly. LES of the noise radiated by a flow over a rectangular cavity. In *ERCOFTAC Workshop on LES for Acoustics*, pages 7–8, 2002.
- [51] X. Gloerfelt, C. Bailly, and D. Juvé. Direct computation of the noise radiated by a subsonic cavity flow and application of integral methods. *Journal of Sound and Vibration*, 266(1):119–146, 2003.
- [52] H. Lai and K. H. Luo. A three-dimensional hybrid LES-acoustic analogy method for predicting open-cavity noise. *Flow, Turbulence and Combustion*, 79:55–82, 2007.
- [53] X. Gloerfelt. Large-eddy simulation of a high Reynolds number flow over a cavity including radiated noise. In *10th AIAA/CEAS Aeroacoustics Conference*, page 2863, 2004.

-
- [54] P. Welch. The use of fast Fourier transform for the estimation of power spectra: a method based on time averaging over short, modified periodograms. *IEEE Transactions on Audio and Electroacoustics*, 15(2):70–73, 1967.
- [55] C. H. K. Williamson. Vortex dynamics in the cylinder wake. *Annual Review of Fluid Mechanics*, 28(1):477–539, 1996.
- [56] G. V. Papaioannou, D. K. P. Yue, M. S. Triantafyllou, and G. E. Karniadakis. Three-dimensionality effects in flow around two tandem cylinders. *Journal of Fluid Mechanics*, 558:387–413, 2006.
- [57] R. Kojima, T. Nonomura, A. Oyama, and K. Fujii. Large-eddy simulation of low-Reynolds-number flow over thick and thin NACA airfoils. *Journal of Aircraft*, 50(1):187–196, 2013.